BACKSCATTER ERROR BOUNDS FOR THE ELASTIC LIDAR TWO-COMPONENT INVERSION ALGORITHM

Francesc Rocadenbosch[1,2], Member IEEE,

Dhiraj Kumar[1,2], Diego Lange[1,2], Eduard Gregorio[3,1], Stephen Frasier[4], and Michaël Sicard[1,2]

ABSTRACT

Total backscatter-coefficient inversion error bounds for the two-component lidar inversion algorithm (the so-called Fernald's or Klett-Fernald-Sasano's method) are derived in analytical form in response to three error sources: (i) the measurement noise, (ii) the user uncertainty in the backscatter-coefficient calibration, and (iii) in the aerosol extinction-to-backscatter ratio.

Two different types of error bounds are presented: Approximate error bounds using first-order error propagation and exact error bounds using a total-increment method. Both error bounds are formulated in explicit analytical form, which is of advantage for practical physical sensitivity analysis and computational implementation. A Monte Carlo approach is used to validate the error bounds at 355-, 532-, and 1064-nm wavelengths.

INDEX TERMS

Lidar, inversion, backscatter coefficient, Fernald's algorithm, signal processing

[1] Remote Sensing Laboratory (RSLab, http://www.tsc.upc.edu/rs/), Department of Signal Theory and Communications, Universitat Politècnica de Catalunya (UPC), Campus Nord, Jordi Girona 1-3, 08034 Barcelona, Spain. Phone: +34-93-401-68-49, FAX: +34-93-401-72-32 (corresponding author e-mail: roca@tsc.upc.edu).

[2] Institute for Space Studies of Catalonia (Institut d'Estudis Espacials de Catalunya) – Aeronautics and Space Research Center (Centre de Recerca de l'Aeronàutica i de l'Espai), Universitat Politècnica de Catalunya, Barcelona, Spain.

[3] Universitat de Lleida (UdL), Dept. of Agroforestry Eng., E-25001 Lleida, Spain

[4] Microwave Remote Sensing Laboratory (MIRSL), Electrical and Computer Eng., University of Massachusetts (UMASS), Amherst, MA, USA.

1. INTRODUCTION

Elastic-backscatter lidars are laser remote-sensing instruments widely used as range-resolved atmospheric probes [1]. Examples are found in ground-based aerosol-observation networks such as the European Aerosol Research Lidar Network (EARLINET) and the Micro-Pulse Lidar Network (MPLNET) among others [2], and in space missions such as the Lidar In-space Technology Experiment (LITE) [3] and, more recently, onboard the CALIPSO satellite (NASA-CNES, 2006) [4].

The lidar equation is inherently underdetermined as it contains two unknowns (the atmospheric extinction and the backscatter coefficient) but only a single observable (the optical power returned as a function of time). Backscatter lidars provide only range-resolved profiles of attenuated backscatter signal [5][6][7]. This under-determination is in contrast to other schemes such as elastic-Raman systems, High Spectral Resolution Lidars (HSRL) [8], and variational multi-angle backscatter-lidar retrievals [9], all of which enable independent inversion of both aerosol extinction and backscatter coefficients [10].

Building on previous works including those of Hitschfeld and Bordan (1951) [11], Barret and Ben-Dov [12], Viezee et al. [13], Davis [14], Fernald [15], Collis and Russell [5], and Kohl [16], in 1981, Klett presented a stable inversion algorithm to invert the elastic single-scattering lidar equation assuming a one-component atmosphere [17] where there is no separation between aerosol and molecular components. In 1984, Fernald presented the two-component version of the algorithm [18], which Klett reformulated in a unified approach [19]. Both Klett's one-component (KLT for short) and Fernald's two-component algorithm (also known as Klett-Fernald-Sasano's method, KFS for short) require additional inputs to resolve the under-determination of the lidar equation. They are, provision of 1) a boundary condition and 2) a range-dependent extinction-to-backscatter ratio. The boundary condition usually consists on a known or

presumed value of the extinction or backscatter coefficient at the far-end of the range profile. This value is used as an absolute calibration for retrieving extinction or backscatter coefficients at lesser ranges. Henceforth, we refer to this simply as the calibration. The extinction-to-backscatter ratio may include both molecular and aerosol effects, or it may include aerosol effects only. Many authors use the term "lidar ratio" to refer to the aerosol-only extinction-to-backscatter ratio. In our development we will make the distinction between the "total" lidar ratio (including molecular effects) and the aerosol-only lidar ratio when necessary.

Methods to assess the calibration for Klett's one-component inversion algorithm were proposed by Klett himself [20][21] and for the two-component algorithm by Sasano and Nakane [22]. Several authors have since carried out sensitivity studies concerning uncertainties in the lidar ratio [23], the impact of assuming a range-independent lidar ratio [24], uncertainties in the calibration [25][26], and the forward/backward stability of these inversion methods as function of the optical depth [27].

Though historically this was not the case, today both one- and two-component inversion algorithms are usually formulated in backscatter-coefficient form. Backscatter coefficient is always the preferred quantity for retrieval as the extinction coefficient is estimated by multiplying the profile of the backscatter coefficient by the assumed extinction-to-backscatter ratio profile used as input to the retrieval. Errors in the assumed lidar ratio may result in larger error-propagated errors [6], especially in situations of a complex layering of aerosols [28]. Kunz [29] and Kovalev [30][31] have proposed alternative variants (not the object of this paper) allowing trustworthy extinction retrievals, where the far-end calibration is replaced by the optical depth of the sounding path or by a near-end calibration and a nephelometer measurement. The synergetic combination of a backscatter lidar with a sun photometer is also extensively used [32]. Furthermore, optimal estimation [33] and adaptive filtering [34][35] methods offer the possibility to incorporate different relevant information (such as optical thickness or spectral radiance measurements

[36]) into the lidar inversion problem and to provide inversion-error indicators. These advanced methods, which usually find applications in the context of global space-borne measurements are, however, more complex.

Despite the fact that from a purely mathematical analysis both the one- and the two-component algorithms yield equivalent solutions, the two-component algorithm is always the preferred one. This is because the KFS algorithm enables use of the aerosol-only lidar ratio, a parameter characterising the microphysical aerosol properties [37]. In constrast, the KLT requires a total lidar ratio including molecular effects. From a physical point of view, the assumption of a constant total lidar ratio is not justified under relatively clear atmospheres. However, for optically thick atmospheres the aerosol component becomes dominant, and the total lidar ratio reduces to the aerosol lidar ratio, which gave rise to the first applications of the one-component algorithm in the 1980's.

This paper concentrates on the two-component backscatter-coefficient inversion algorithm and is the fifth in a series [38][39][40][41] from the RSLAB related to study the behaviour and error sensitivity of the one- and two-component algorithms. The work presented here first contributes a comprehensive analytical approach in explicit mathematical form merging into a single body all the main error sources involved in the KFS inversion of the aerosol backscatter coefficient. These include: 1) systematic errors due to uncertainties in the calibration, 2) systematic errors due to a range-dependent aerosol lidar ratio, and 3) random errors due to finite signal-to-noise ratio (SNR) in the opto-electronic receiver of the lidar system at all ranges except that of the calibration, and 4) random errors due to finite SNR at the calibration range. The latter two sources of error are considered separately as it was shown in [39] that source 4) dominates.

Errors in the backscatter-coefficient calibration (error source 1) and in the assumed lidar-ratio (error source 2) are systematic errors as they induce biases in the retrieval once encountered. These are in contrast to the random errors induced by noise (error sources 3 and 4). However, since no "a priori"

knowledge of either the magnitude or the sign of the calibration and lidar-ratio errors is assumed, they are treated as drawn from independent probability distribution functions (p.d.f.), usually Gaussian or uniform. While the assumption of a uniform p.d.f. assumes no “a priori” knowledge of the calibration (just that the systematic deviation has constant probability over the width of the p.d.f.) the Gaussian distribution assumes the well-known bell-shaped probability distribution, i.e., a higher likelihood towards the mean value of the distribution or “most likely” assumed calibration.

This paper finds the backscatter-coefficient error bounds for the KFS algorithm explicitly in both approximate and exact forms. Two different sets of explicit error bounds are introduced: first-order derivative error bounds (approximate), which are the KFS counterpart of those found for the KLT algorithm in [40]) and, total-increment error bounds (exact) for the dominant error sources (1, 2 and 4 above). These characteristics are new to the state of the art in the lidar community. The error bounds presented are validated using Monte Carlo techniques at multiple wavelengths of 355 nm (UV), 532 nm (VIS), and 1064 nm (NIR).

This paper is organised as follows: In Sect. 2 the KFS inversion algorithm is reviewed and reformulated in both backward and forward form. In Sect. 3 first-order error bounds via a stochastic approach (error variance propagation) are presented. From this basis, in Sect. 4 total-increment (i.e., exact) error bounds are obtained for the dominant error sources. In Sect. 5, both first-order and total-increment error bounds are cross-examined and validated using a Monte Carlo method. The assumption of a Gaussian versus a uniform p.d.f. for the aerosol lidar ratio – a most difficult atmospheric parameter to estimate due to the changing aerosol composition with height - is discussed in Sect. 5.3. Finally, concluding remarks are given in Sect. 6.

2. REVIEW OF THE KFS TWO-COMPONENT ALGORITHM

2.1. Review of KFS algorithm

Klett-Fernald-Sasano's inversion algorithm is formulated in backward backscatter-coefficient form as

$$\beta^{aer}(R)=\frac{\left[R^2P(R)\right]\exp\left\{2\int_R^{R_m}\left[S^{aer}(u)-S^{mol}\right]\beta^{mol}(u)du\right\}}{\frac{\left[R_m^2P(R_m)\right]}{\beta^{aer}(R_m)+\beta^{mol}(R_m)}+2\int_R^{R_m}S^{aer}(u)\left[u^2P(u)\right]\exp\left\{2\int_u^{R_m}\left[S^{aer}(v)-S^{mol}\right]\beta^{mol}(v)dv\right\}du}-\beta^{mol}(R), \tag{1}$$

where $P(R)$ is the single-scattering optical-return lidar power, R is the range along sight, $S^{aer}(R)$ and $S^{mol}=8\pi/3$ are the aerosol and the molecular (Rayleigh) lidar ratios, respectively, $\beta^{aer}(R)$ and $\beta^{mol}(R)$ are the aerosol and molecular backscatter components, and R_m ($R\le R_m$) is the calibration range. In (1) note that in spite of the two-component separation, the term $\beta(R_m)=\beta^{aer}(R_m)+\beta^{mol}(R_m)$ represents the total backscatter coefficient. In practical tropospheric applications, the calibration range is usually chosen in an atmospheric molecular reference range aloft where the aerosol backscatter component becomes negligible ($\beta^{aer}(R_m)<<\beta^{mol}(R_m)$), consequently, $\beta(R_m)\approx\beta^{mol}(R_m)$.

2.2. Modified backward KFS form

In what follows the aerosol and the molecular backscatter coefficients are assimilated into the total backscatter coefficient, $\beta(R)=\beta^{aer}(R)+\beta^{mol}(R)$, and errors on the molecular backscatter coefficient are neglected so that

$$d\beta^{aer}(R)=d\beta(R). \tag{2}$$

This is justified because the molecular component can be assumed to be very well known. In practice, the atmospheric molecular component is estimated from local temperature/pressure radio-sounding measurements or a US-standard atmosphere model given ground-level temperature and pressure data [42]. Therefore, when calibrating in an atmospheric layer dominated by molecular scattering,

$$\beta_N = \beta(R_N) = \beta^{aer}(R_N) + \beta^{mol}(R_N) \approx \beta^{mol}(R_N). \tag{3}$$

By introducing the discrete range, $R_j = R_{\min} + (j-1)\Delta R, \quad j = 1..N$, with ΔR the spatial resolution of the lidar data and N the number of range samples (or cells) to be inverted, (1) can be rewritten in discrete form as

$$\beta_j(\beta_N, \vec{S}, \vec{U}) = \frac{\beta_N U_j F_j(\vec{S})}{U_N + 2\beta_N H_j(\vec{S}, \vec{U})}, \tag{4}$$

where U_j, F_j and H_j are shorthand for $U(R_j)$, $F(R_j)$ and $H(R_j)$, which are auxiliary functions evaluated for each range, and the vector $\vec{S}$ is the range-dependent aerosol lidar ratio, $S^{aer}(R_j)$. The auxiliary functions U_j, F_j and H_j are defined as

$$U_j = R_j^2 P(R_j), \tag{5}$$

$$F_j(\vec{S}) = \exp[2G_j(\vec{S})], \tag{6}$$

where

$$G_j(\vec{S}) = \begin{cases} \sum_{i=j}^{N} w_i (S_i^{aer} - S_i^{mol}) \beta_i^{mol} & j < N \\ 0 & j = N \end{cases}, \tag{7}$$

and

$$H_j(\vec{S}, \vec{U}) = \sum_{i=j}^{N} w_i S_i^{aer} U_i F_i(\vec{S}). \tag{8}$$

In (7)-(8), the w_i, $i = 1..N$ denote generic integration weights (e.g., $w_i = h = 1, \quad i = 1..N-1; \quad w_N = 0$ in the case of rectangle integration, which requires $N \geq 2$ points). The notation $\beta_j\left(\beta_N, \vec{S}, \vec{U}\right)$ is a reminder that the total backscatter coefficient inverted at the range cell, R_j, depends upon the total backscatter coefficient at the far-range calibration range, β_N, the user-input range-dependent aerosol lidar ratio, $\vec{S}$, and the range-corrected power, $\vec{U}$. In what follows superscript "aer" for the aerosol lidar ratio is omitted so that $\vec{S}$ refers to $\vec{S}^{aer}$, and the "aerosol lidar ratio" is simply addressed as "the lidar ratio".

2.3. Comparison with Klett's one-component algorithm

When comparing KLT versus KFS equations (5)-(6) in [40] with Eqs. (4), (6) and (8) above, the KLT-to-KFS correspondence Tab. 1 is obtained. The U_j into $U_j F_j\left(\vec{S}\right)$ relationship agrees with previous published results (Tab. 1 in [41]) and the $G_j\left(\vec{S}, \vec{U}\right)$ into $H_j\left(\vec{S}, \vec{U}, \vec{F}\right)$ is a new relationship completing the transformation.

2.4. Forward case

In the forward-integration form of the KFS algorithm (i.e., calibration range located at the near end of the inversion range) the far-end calibration at $R = R_N$ is replaced by the near-end calibration $R = R_1$, (i.e., $\beta_N \to \beta_1$) in (4), and $\sum_{i=j}^{N}(.)$ is replaced by $-\sum_{i=1}^{j}(.)$ in all subsequent formulas. In so doing, (4) for the forward case becomes

$$\beta_j\left(\beta_1, \vec{S}, \vec{U}\right) = \frac{\beta_1 U_j F_j^F\left(\vec{S}\right)}{U_1 + 2\beta_1 H_j^F\left(\vec{S}, \vec{U}\right)}, \tag{9}$$

where $F_j^F\left(\vec{S}\right)=\exp\left(2G_j^F\right)$ after (6) and G_j^F and H_j^F are defined following (7)-(8) above but replacing $\sum_{i=j}^{N}(.)$ by $-\sum_{i=1}^{j}(.)$, as mentioned. This leads to the well-known classic forward form including a minus sign in front of the factor of 2 in the denominator and in the exponential arguments of (1). Note also that the minus sign arising from the change of summations above is algebraically equivalent to substituting $S^{aer}\rightarrow -S^{aer}$ and $S^{mol}\rightarrow -S^{mol}$ into the KFS backward form of (4). This also accounts for the opposite signs of the backscatter-to-lidar-ratio derivatives of the forward/backward forms (Sect. 4.2).

3. FIRST-ORDER BACKSCATTER-COEFFICIENT ERROR BOUNDS

3.1. Overview: The error-propagation approach

This section parallels Sect. 3 of [40] where the backscatter-coefficient error bounds are computed from the superposition of error sources 1-4 (Sect. 1) using a first-order derivative approach. Following (7) in that work,

$$\begin{cases} \left|d\beta_j\right|=\left|\dfrac{\partial\beta_j}{\partial\beta_N}d\beta_N\right|+\sum_{k=1}^{N}\left|\dfrac{\partial\beta_j}{\partial S_k}dS_k\right|+\sum_{k=1}^{N-1}\left|\dfrac{\partial\beta_j}{\partial P_k}dP_k\right|+\left|\dfrac{\partial\beta_j}{\partial P_N}dP_N\right|; & j<N \\ \left|d\beta_j\right|=\left|d\beta_N\right|; & j=N \end{cases}, \qquad (10)$$

where $d\beta_j$ is the total backscatter coefficient error at range, R_j, and $d\beta_N$, dS_k, dP_k, and dP_N, respectively stand for error sources (1)-(4).

For the case $j<N$ the terms $\dfrac{\partial\beta_j}{\partial\beta_N}$, $\dfrac{\partial\beta_j}{\partial P_k}$ and $\dfrac{\partial\beta_j}{\partial P_N}$ can be readily computed from (8), (10)-(11) in [40] and the function substitutions indicated in the KLT-to-KFS transformation Tab. 1. Yet, this

procedure cannot be followed when computing the errors due to the lidar ratio, $\frac{\partial \beta_j}{\partial S_k}$, as the KFS auxiliary functions F_j and H_j (6, 8) also depend on the lidar ratio. This case is revisited in the Appendix. The case $j = N$ in (10) expresses the assumed error on the backscatter-coefficient calibration. Finally, the terms comprising (10) and denoted $\varepsilon_{j,1-4}$ are detailed in Tab. 2.

3.2. Computation: The stochastic approach

The treatment of systematic and random error sources as independent probability distribution functions (Sect. 1) enables a common stochastic approach. The stochastic approach assumes that error sources $d\beta_N$ (backscatter-coefficient calibration error), dS_k (lidar-ratio error) and dU_k (range-corrected random noise perturbation, (5)) are independent Gaussian random variables with standard deviations, σ_{β_N}, σ_{S_k}, and σ_{U_k}, respectively. Following [43], the total error is found by adding all of the errors in mean square since they have independent distributions. The backscatter-coefficient total-error standard deviation is given in (34), Tab. 3. Computation of the error standard deviation $\sigma_{\varepsilon_{j,1}}$, which is due to the backscatter-coefficient calibration, and $\sigma_{\varepsilon_{j,3-4}}$, due to the measurement noise, from Tab. 2 is straightforward once Tab. 1 and the procedures described in [40] (Sect. 3B and Tab.1, p.3386) are followed. At this point, note that $G_N = 0$ and $F_N = 1$ (Eqs.(6)-(7)) and that, when considering error sources 3 and 4, $d(U_k F_k) = F_k dU_k, k = 1..N$, because the only "fluctuating" variable due to noise is the range-corrected power, U_k. As previously mentioned, computation of the lidar ratio, $\sigma_{\varepsilon_{j,2}}$, requires a specific analysis for the KFS algorithm. At this point a few comments are in order:

First, regarding errors due to the backscatter-coefficient calibration ($\sigma_{\varepsilon_{j,1}}$) and those due to the measurement noise at the calibration cell ($\sigma_{\varepsilon_{j,4}}$), it is evident from (35) and (46), Tab. 3 that both error sources can be related as

$$\frac{\sigma_{\varepsilon_{j,1}}}{\sigma_{\varepsilon_{j,4}}} \approx \left|\frac{U_N}{\beta_N}\right| \frac{\sigma_{\beta_N}}{\sigma_{U_N}} = \mathrm{SNR_N} \varepsilon_r^{\beta_N} \quad . \tag{11}$$

Here, $\varepsilon_r^{\beta_N} = \sigma_{\beta_N} / \beta_N$ is the relative error in the backscatter-coefficient calibration, and SNR_N is the SNR at the calibration range, $R = R_N$. A similar relationship is found in Eq. (28) in [40], therefore, the effects of these two error sources on the inverted backscatter coefficient are qualitatively the same on both KLT and KFS algorithms.

Next, regarding errors due to the measurement noise ($\sigma_{\varepsilon_{j,3}}$ and $\sigma_{\varepsilon_{j,4}}$), from (44) the backscatter-coefficient error on the j-th range cell is inversely proportional both to the SNR at that cell, $SNR_j = U_j / \sigma_{U_j}$, and to a "cross-cell SNR" defined as $SNR_{j,k} = U_j / \sigma_{U_k}$. A similar dependence was observed in [39] and [40] and earlier by Knauss [44], who predicted an inverse SNR sensitivity. Concerning $\sigma_{\varepsilon_{j,4}}$, (46) can be rewritten as $\sigma_{\varepsilon_{j,4}} \approx \left|\frac{\beta_j^2 U_N}{\beta_N U_j F_j}\right| \frac{1}{SNR_N}$ (see similar justification steps in [40], p. 3383). It emerges that a finite SNR at the calibration range propagates errors to all the range cells.

Third, regarding error due to a range-dependent lidar ratio ($\sigma_{\varepsilon_{j,2}}$), a useful assumption in practice is to define a systematic lidar-ratio relative error, p relating the range-dependent lidar-ratio error and the true atmospheric lidar ratio as [40]

$$dS(R) = pS(R) \Leftrightarrow dS_k = pS_k \,. \tag{12}$$

Equivalently, the atmospheric lidar ratio is assumed to lie within $S(R)(1\pm|p|)$ at 1-σ confidence level. Error bound computation uses first-order series expansion of (4) around p. Towards this end (4) is rewritten as a function of lidar-ratio perturbation p as

$$\beta_j(p)=\frac{\beta_N\, U_j F_j(p)}{U_N+2\beta_N\, H_j(p)}, \tag{13}$$

where the incremental auxiliary function $F_j(p)$ is related to $G_j(p)$ via (6), and $G_j(p)$ and $H_j(p)$ from (7)-(8) become

$$G_j(p)=\begin{cases}(1+p)I_{j,1}-K_j; & j<N\\ 0 & j=N\end{cases}, \tag{14}$$

where

$$I_{j,1}=\sum_{i=j}^{N} w_i\beta_i^{mol}S_i^{aer}, \quad K_j=\sum_{i=j}^{N} w_i\beta_i^{mol}S_i^{mol}, \tag{15}$$

and

$$H_j(p)=(1+p)\sum_{i=j}^{N} w_i S_i^{aer}U_i F_i(p). \tag{16}$$

From (14)-(15) above (6), $F_j(p)$ takes the form

$$F_j(p)=\exp\lfloor 2G_j(p)\rfloor = F_j(0)\exp(2pI_{j,1}). \tag{17}$$

Finally, the backscatter-coefficient error is obtained after first-order series expansion as

$$\sigma^C_{\varepsilon_{j,2}}=\left|d\beta_j^S\right|\approx\left|\left.\frac{\partial\beta_j}{\partial p}\right|_{p=0} p\right|, \tag{18}$$

where superscript “C” denotes “correlated” and superscript “S” denotes “due to the lidar ratio”. (18) is computed by substituting the proportionality condition of (12) into the general expression of the propagated

lidar-ratio error, $\varepsilon_{j,2}$ (Eqs.(28)-(31)). The result is summarised in Tab. 3 and yields symmetrical error bounds.

A less realistic model for lidar-ratio errors is to assume they are uncorrelated from range cell to range cell (i.e., $E\lfloor dS_i dS_j \rfloor = 0, i \neq j$) [40]. Such uncorrelated errors can average out during KFS integration. As a result, a lower backscatter-coefficient error bound, $\sigma_{\varepsilon_{j,2}}$ is obtained (Tab. 3). Its calculus departs from (28)-(31), and interprets lidar-ratio errors, dS_k, as uncorrelated random variables with variances $\sigma_{S_k}^2$ $(k = 1..N)$.

4. TOTAL INCREMENT BACKSCATTER COEFFICIENT ERROR BOUNDS

Total-increment error bounds stand for infinite order, or equivalently, exact error bounds. The procedure is conceptually simple for it reduces to compute the total error, $\beta_j(x \pm \Delta x) - \beta_j(x)$, where x is the variable of interest. In what follows, Δx refers to a generic input error $d\beta_N$ (backscatter-coefficient calibration error), dS_k (lidar-ratio error) or dU_k, $k = 1..N$ (range-corrected noise-induced error, Sect. 3), alternatively, to the input uncertainty on these error sources at a prescribed n-σ level (usually at 3-σ level).

Under moderate-to-high SNRs assuming that error sources 1-4 are independent Gaussian random variables does not compromise the fact that the backscatter-coefficient error, $d\beta_j$ ((10), Tab. 2) also follows a Gaussian distribution. Thus, the first-order error propagation approach of Tab. 2 is just a perturbational approach simply scaling the input errors by partial derivatives to estimate the total backscatter-coefficient error. In contrast, under low SNRs and/or when the user's uncertainty of the algorithm inputs ($\lfloor x - \Delta x, x + \Delta x \rfloor$) is comparatively large, first-order derivative error bounds fail to correctly estimate the backscatter-coefficient error, as this error is no longer Gaussian distributed.

Therefore, total-increment error bounds provide a convenient way to compute exact upper and lower error bounds (usually with asymmetrical amplitudes around the true backscatter value) in explicit form.

4.1 Error source 1: Error due to the backscatter-coefficient calibration ($d\beta_N$)

From (27) it emerges that the derivative of the inverted backscatter coefficient with respect to the backscatter-coefficient calibration is always positive, $\frac{\partial \beta_j}{\partial \beta_N} > 0$, since $\beta_j, \beta_N, U_j, U_N$ and F_j are positive-defined magnitudes. As a result, $\beta_j\left(\beta_N \pm d\beta_N\right) = \beta_j \pm d\beta_j$ (plus and minus signs are one-to-one maintained) and the total-increment error bounds of (48) result.

4.2 Error source 2: Error due to the range-dependent lidar ratio (correlated case)

From (4) the incremented backscatter-coefficient function can be expressed as

$$\beta_j\left(\vec{S}+d\vec{S}\right) = \frac{\beta_N\, U_j F_j\left(\vec{S}+d\vec{S}\right)}{U_N + 2\beta_N\, H_j\left(\vec{S}+d\vec{S},\vec{U}\right)} \xrightarrow{d\vec{S}=p\vec{S}} \beta_j(p) = \frac{\beta_N\, U_j F_j(p)}{U_N + 2\beta_N\, H_j\left(p,\vec{U}\right)}. \quad (19)$$

In the correlated case, the lidar-ratio increment $d\vec{S}$ is related to the lidar ratio $\vec{S}$ via the relative error p so that $d\vec{S} = p\vec{S}$ (Eq. 12). As a result, the incremental term $\left(\vec{S}+d\vec{S}\right)$ (equivalently, $\vec{S}(1+p)$) becomes only a function of the scalar relative error p and (19) reduces to (13). Incremental auxiliary functions $F_j(p)$ and $H_j\left(p,\vec{U}\right)$ can be computed from (6) and (8), respectively.

The sign of the backscatter-coefficient's derivative with respect to the lidar-ratio relative error, $\frac{\partial \beta_j}{\partial p}$, at each particular range R_j determines whether the upper and lower backscatter-coefficient error bounds at each range cell are respectively obtained from $\beta_j(p)$ (i.e., $\beta_j\left(\vec{S}+d\vec{S}\right)$) and $\beta_j(-p)$ (i.e.,

$\beta_j\left(\vec{S}-d\vec{S}\right)$) or with opposite signs. For the backward integration case this derivative is obtained following a somewhat lengthy but similar development to that of $\left.\frac{\partial\beta_j}{\partial p}\right|_{p=0}$ in (18) and (36). Formally,

$$\frac{\partial\beta_j^B}{\partial p}=2\beta_j^B(p)I_{j,1}^B-\frac{2\beta_j^B(p)^2}{U_jF_j^B(p)}\left[I_{j,2}^B(p)+2(1+p)I_{j,3}^B(p)\right],\quad j<N, \tag{20}$$

where $I_{j,1-3}^B$ is given by (37)-(39) in Tab. 3. The result is identical for the forward integration case ($j>1$) with superscripts "F" (forward) instead of "B" (backward). Note that forward integrals $I_{j,1-3}^F$ must include a minus sign according to Sect. 2.4.

We note that a more elegant and physically-rooted way to identify the sign of the backscatter-coefficient derivative to the lidar-ratio relative error is to recall that in forward (backward) integration the inverted backscatter coefficient at any range increases (decreases) with the lidar ratio (Fig. 1). This property is the basis of the two-point lidar-ratio estimation method in an aerosol layer aloft using combined forward/backward integration ([10], p.7123 and detailed in [45]). The derivative of the backscatter coefficient with respect to the lidar ratio is obviously zero at the calibration point. In summary,

$$\frac{\partial\beta_j^F}{\partial p}>0,\ \frac{\partial\beta_j^B}{\partial p}<0,\quad \forall p,j,\ \left.\frac{\partial\beta_j^F}{\partial p}\right|_{j=1}=0,\ \left.\frac{\partial\beta_j^B}{\partial p}\right|_{j=N}=0,\quad \forall p, \tag{21}$$

which is a condition applying to any range R_j. Therefore, $\beta_j\left(\vec{S}\pm d\vec{S}\right)=\beta_j\pm d\beta_j$ in the forward case whereas $\beta_j\left(\vec{S}\pm d\vec{S}\right)=\beta_j\mp d\beta_j$ in the backward case (Tab. 4).

4.3 Error sources 3-4: Errors due to the measurement noise

As discussed in Sect. 1, the impact of measurement noise in the KFS algorithm has been studied in [41]. In spite of the fact that exact backscatter-coefficient error bounds satisfying a constant confidence

level are given analytically, its formulation is in implicit form. This means that given a confidence level, two auxiliary integrals ((9) and (12) in [41]) and two integral equations ((18) and (19) in [41]) must be solved for each range of interest. This yields two error bounds, which are later used to compute the upper and lower backscatter-coefficient error bounds.

Explicit formulation of total-increment error bounds is hampered by the fact that the measurement noise is usually uncorrelated with range, i.e., each range cell along the inversion range contributes independent error amounts dU_j, $j = 1..N-1$. This leads to the superposition of $N-1$ noise sources, that is, to an $(N-1)$-dimensional problem impeding any explicit formulation of the total-increment error bounds in Tab. 4.

Hovewer, because of the comparatively larger impact of error source 4 (see NIR grounds in [41] and results in Sect. 5.1.3) the first-order error bound, $\sigma_{\varepsilon_{j,3}}$, given by (44), represents a very good approximation of an already small quantity. A final remark is that the first term of the error-propagated backscatter-coefficient derivative, $\varepsilon_{j,3} \approx \frac{\beta_j}{U_j} dU_j$ (Eq.(32)) does represent the total increment $\beta_j\left(\vec{U} + d\vec{U}\right) - \beta_j\left(\vec{U}\right)$ if $H_j\left(\vec{S}, \vec{U}\right)$ (Eq.(8)) is assumed to be nearly independent of fluctuations in $\vec{U}$. This is indeed the case, because range-corrected power fluctuations tend to smooth out with range during forward/backward integration.

Finally, the error due to the measurement noise at the calibration cell is analogous to that of Sect. 4.1, except for the fact that now the derivative of the inverted backscatter coefficient to the power at the calibration range is always negative, $\frac{\partial \beta_j}{\partial P_N} < 0$ (33). The error bounds are given in (53), Tab. 4.

5. DISCUSSION

First-order error bounds (Tab. 3) and total-increment error bounds (Tab. 4) are validated here using a multi-wavelength Monte Carlo (MC) approach at 355-nm (UV), 532-nm (VIS) and 1064-nm (NIR) wavelengths. In the MC simulation, for each wavelength, a set of 100 profiles of the aerosol backscatter coefficient has been inverted given 100 noise corrupted lidar power returns realized from a synthetic backscatter atmospheric profile and a range-dependent SNR profile (Fig. 2).

To make the simulation more realistic, the shape of the profile of the aerosol backscatter coefficient has been obtained from a 532-nm inversion of a measurement record obtained with the RSLAB lidar (slant path, 54-deg elevation angle). The 355- and 1064-nm aerosol backscatter components have been extrapolated from the inverted one at 532 nm assuming a λ^{-1} spectral dependency. The molecular backscatter component follows a U.S. standard atmosphere model [42] (15ºC and 1013.15 hPa ground-level conditions) and a λ^{-4} spectral dependency. A mean total extinction, $\overline{\alpha} \approx 2 \times 10^{-4} m^{-1}$ at 532 nm, corresponding to a total optical depth, $\tau \approx 1.2$, over the slant sounding path, is simulated. In order to study error sources 1-4 in identical simulation conditions, a wavelength-independent lidar ratio, $S^{aer} = 50 sr$ is used, and the simulated measurement noise level is adjusted so as to ensure a SNR of 5 at the maximum range (a relatively modest figure in practice), in all three lidar channels. The inversion interval ranges from $R_{\min} = 0.2 km$ to a maximum range, $R_{\max} = 6 km$. The calibration range is chosen at $R_{cal} = R_{\max} = 6 km$, where the lidar return is dominated by molecular scattering. The atmospheric boundary layer, characterized by significant aerosol backscatter, ends at approximately 5 km range.

Lidar system parameters used for the simulation are based on the new MRL (Multi-spectral elastic-Raman Lidar) of the RSLAB (40/130/130-mJ energy at 355/532/1064-nm wavelength, respectively, 3.6-ns pulse width, Nd:YAG laser source; 35.5-cm aperture, 3.9-m focal-length telescope). UV and VIS channels are PMT (Photo-Multiplier Tube) based with an approximate reception channel NEP (Noise Equivalent

Power), $NEP_{355,532} = 7.7 \times 10^{-15} \left[W \cdot Hz^{-1/2} \right]$ while the NIR channel is APD (Avalanche Photo-Diode) based with approximate channel $NEP_{1064} = 9.3 \times 10^{-13} \left[W \cdot Hz^{-1/2} \right]$. The SNR model used is described in [46], Annex A, and assimilates signal-shot photo-induced, dark-shot, and thermal noise components into a single range-dependent noise-equivalent variance.

Backscatter-coefficient plots are visible-wavelength normalised (VIS-normalised) to aid intercomparison at the three wavelengths. Thus, UV and NIR profiles of the inverted backscatter coefficient are scaled by $(\lambda_{532}/\lambda_{355})^{-1}$ and $(\lambda_{532}/\lambda_{1064})^{-1}$ factors, respectively. A VIS-normalised Fig. 2(a) would appear with UV, VIS and NIR traces all coincident (figure not shown).

5.1. Error sources 3-4: Errors due to the measurement noise

5.1.1 Noise in all range cells except the calibration cell ($\sigma_{\varepsilon_{j,3}}$ in Tab. 3, $\varepsilon_{j,3}^{u/l}$ in Tab. 4).

According to the superposition principle the simulation runs with $SNR(R)$ *for* $R \neq R_{cal}$, Fig. 2b, and all other error sources inactive. That is, $SNR(R_{cal}) \to \infty$ (no noise on the return power at the calibration cell, error source 4), perfect backscatter-coefficient calibration (error source 1), and known atmospheric lidar ratio (error source 2).

Fig. 3a plots the envelopes of the family of the MC-inverted profiles of the aerosol backscatter coefficient along with first-order error bounds (Eq.(44), Tab. 3) computed at 3σ (error bounds are plotted as vertical bars centered in the input "true" profile of the atmospheric backscatter coefficient) while Fig. 3b compares their error amplitudes. The error amplitudes represent the difference between the upper and lower backscatter-coefficient error bounds and the true profile of the atmospheric backscatter coefficient. In Fig. 3b, upper and lower MC error bounds superimpose and appear as a single noisy trace -at each wavelength-. Because of the first-order series expansion, first-order error bounds are always symmetric. Besides, Fig. 3b

shows perfect agreement between both MC and first-order error bounds at all wavelengths. This is of advantage in order to approximate the total-increment error bound $\varepsilon_{j,3}^{u/l}$ (not found for this error source) as $\varepsilon_{j,3}^{u/l} \approx 3\sigma_{\varepsilon_{j,3}}$ in Tab. 4.

Fig. 3 shows that errors increase with range in response to a progressively decreasing range-dependent SNR (Fig. 2b) and also increase towards the UV. An explanation for that is that the $\sigma_{\varepsilon_{j,3}}$ term $\left(\beta_j / U_j\right)\sigma_{U_j} = \beta_j / SNR_j$ in (44), Tab. 3 is inversely proportional to the SNR and directly proportional to the backscatter coefficient. Towards the UV, $\sigma_{\varepsilon_{j,3}}$ increases due to the higher scattering in this band and a lower SNR (Fig. 2b). As mentioned in Sect. 4.3, the term $\sigma_{HU,j}$ ((45)) becomes numerically much lower because noise averages out when integrating.

5.1.2 Noise in the calibration cell ($\sigma_{\varepsilon_{j,4}}$ in Tab. 3, $\varepsilon_{j,4}^{u/l}$ in Tab. 4).

Simulation conditions are analogous to those used for the error source 3 above except that now $SNR(R_{cal}) = SNR_N = 5$ and $SNR(R) \to \infty,\ R \neq R_{cal}$. Fig. 4a shows that the effects of the measurement noise at the calibration cell propagate down to all the inversion cells and are comparatively larger in the NIR. Thus, while in the NIR, errors tend to amplify progressively backwards with range (up to 1.8 km approximately), in the UV, they reduce backwards with range (see analogous behaviour for error source (1), Sect. 5.2). Fig. 4b shows fairly good agreement between first-order error bounds ($\sigma_{\varepsilon_{j,4}}$ in Tab. 3) and MC error bounds, evidenced by the former falling in between upper and lower MC error bounds. In contrast to what happened when studying the error source (3), MC error bounds are no longer symmetric. An explanation for that is that noise at the calibration range tends to be the dominant error source ($\sigma_{\varepsilon_{j,4}} \geq \sigma_{\varepsilon_{j,3}}$ over the whole inversion range), hence causing that larger backscatter-coefficient errors cease

to be Gaussian distributed [39]. By comparing Fig. 4b and Fig. 3b, the impact of noise at the calibration range is more prominent towards the NIR. Thus, in the UV, $\sigma_{\varepsilon_{j,4}} \approx \sigma_{\varepsilon_{j,3}}$ (this distinguishing feature was not identified in earlier work as it was conducted at 1064 nm). A mathematical hint for that comes from the ratio between these two noise-induced error sources, $\frac{\sigma_{\varepsilon_{j,4}}}{\sigma_{\varepsilon_{j,3}}} \approx \frac{\beta_j}{\beta_N}\frac{1}{F_j}\frac{\sigma_{U_N}}{\sigma_{U_j}}$ (Eqs. (44)-(46)), where -by experiment- it has been found that $\left(\frac{2\beta_j^2}{U_j F_j}\right)^2 \sigma_{HU,j}^2 << \left(\frac{\beta_j}{U_j}\right)^2 \sigma_{U_j}^2$ in (44). Because of the higher molecular component in the UV, the ratio β_j/β_N (recall that β stands for the "total" backscatter coefficient and that β_N is calibrated in a purely molecular reference range, Sect. 2.1) is much smaller in the UV than in the NIR, thus enabling $\sigma_{\varepsilon_{j,3}}$ and $\sigma_{\varepsilon_{j,4}}$ to become comparable in the UV. Total-increment error bounds $\varepsilon_{j,4}^{u/l}$ at 3σ (Tab. 4) perfectly match upper and lower MC error bounds in Fig. 4b and superimpose with them.

5.1.3 Superposition of error sources 3- 4 ($\sigma_{\varepsilon_{j,3-4}}$ in Tab. 3, $\varepsilon_{j,3-4}^{u/l}$ in Tab. 4)

First-order error bounds ($\sigma_{\varepsilon_{j,3-4}}$) and total-increment error bounds ($\varepsilon_{j,3-4}^{u/l}$) are compared with the implicit integral ones from previously published results (Sect. 4.3). All three types of error bounds are computed at 3σ ($p = 99.73\%$ probability that an inverted backscatter-coefficient realization falls within the error bounds). To compute first-order error bounds $3\sigma_{\varepsilon_{j,3-4}}$, Tab. 3 is used. To compute total-increment error bounds, $\varepsilon_{j,3}^{u/l}$, Eq.(52) approximation, Tab. 4 is used and, obviously, the exact Eq.(53) with $dU_N = 3\sigma_{U_N}$ is used to compute $\varepsilon_{j,4}^{u/l}$.

Because upper and lower integral error bounds must be solved for each range cell and the solutions become numerically ill-conditioned for dense atmospheres ($\tau > 2$, approximately), they have only been computed for a discrete set of six ranges, from 1 to 6 km, equi-spaced 1 km. In nearly all the simulation

runs the upper and lower MC error bounds computed with 100 lidar signal realizations coincided with the integral error bounds (i.e., the exact theorical reference). Thus, the MC error bounds can be considered reliable bounds of the 3-σ inverted backscatter-coefficient population and, therefore, equivalent trustworthy extrapolations of the integral "exact" error bounds over all the range cells.

Multi-wavelength performance of both first-order and total-increment error bounds with reference to the implicit integral error bounds is shown in Fig. 5. Fig. 5a shows a comparatively poorer but still fairly good performance of the first-order error bounds, which give error bound amplitudes in between those of the MC error bounds or slightly closer to the MC lower error bound (the upper MC error bound in the NIR falls below the implicit integral error bound as a consequence of the natural statistical dispersion in this specific simulation run and wavelength). Fig. 5b shows that total-increment error bounds give virtually identical estimates that the implicit-integral error bounds with the advantage of being formulated in explicit form, being simpler to compute, and providing range-resolved information. The mean backscatter-relative error between both types of error bounds is below 1.7% in the UV, 0.6 % in the VIS, and 0.5% in the NIR, this difference being only due to Eq.(52) approximation. The spectral behaviour of Fig. 5 is analogous to that of Fig. 4b.

5.2. Errors due to the backscatter-coefficient calibration ($\sigma_{\varepsilon_{j,1}}$ in Tab. 3, $\varepsilon_{j,1}^{u/l}$ in Tab. 4)

The behaviour of this error souce is qualitatively identical to that of the noise at the calibration range (error source (4), Fig. 4) – hence, analogous plots are retrieved (figure not shown)- for according to (11) the error standard deviation of these two error sources on the inverted backscatter coefficient ($\sigma_{\varepsilon_{j,1}}$ and $\sigma_{\varepsilon_{j,4}}$, respectively) can be related to one anoher by a scaling factor $C = \mathrm{SNR_N}\varepsilon_r^{\beta_N}$. That is, the error-bound amplitude plots for this error source (1) become Fig. 4b scaled by $C = 0.5$ when a relative backscatter-calibration error $\varepsilon_r^{\beta_N} = \sigma_{\beta_N} / \beta_N = 0.1$ is simulated ($SNR_N = 5$ in Fig. 4a). Therefore, identical

conclusions apply, specifically, that the backscatter-coefficient calibration error becomes dominant in the NIR. This is best corroborated in Fig. 6, which uses a step-function atmospheric backscatter-coefficient profile with a 1-km falling edge between 4-5 km simulating the end of the boundary layer, and an error strength, $\varepsilon_r^{\beta_N} = 0.1$. In the mixing layer (0.2-4-km range) the error bound amplitudes can be ranked NIR > VIS > UV, as expected.

5.3. Errors due to the lidar ratio ($\sigma^C_{\varepsilon_{j,2}}$ in Tab. 3, $\varepsilon^{u/l}_{j,2}$ in Tab. 4)

Simulation conditions for this case assume noiseless power lidar returns ($SNR(R) \to \infty$ in all range cells), perfect backscatter-coefficient calibration, and correlated lidar-ratio errors defined by a relative error figure, p, which is simulated both as Gaussian random variable with standard deviation $p = 10\%$ and $p = 30\%$ (3-σ deviation equal to 30% and 90%, respectively) and also as uniform random variable with standard deviation $p' = 3p$ so as to ensure similar error spans in both probability distributions. During the tests, (20) and (21) gave always the same signs, as expected.

Fig. 7 shows the performance of the total-increment error bounds, which perfectly match MC error bounds. For small errors (p =10%, which corresponds to a uniform error span of ±30%, figure not shown) the total-increment upper and lower error bounds tend to distribute symmetrically around the "true" atmospheric backscatter coefficient, that is, which similar upper and lower error amplitudes. This is no longer the case for larger errors (p =30%, which corresponds to a uniform error span of ±90%). The inverted backscatter-coefficient error bounds and their asymmetry increases towards the UV, which reinforces the fact that lidar ratio uncertainties become more critical towards the UV.

In Fig. 8 total-increment and first-order error bounds are compared assuming both Gaussian and uniform distributions for the lidar-ratio uncertainties. Total-increment error bounds perfectly match the error span of the family of inverted profiles of the backscatter coefficient when the uncertainty of the lidar

ratio follows a uniform distribution (Fig. 8a). In contrast, first-order error bounds at 3-σ, which are of smaller amplitude, are best to encompass most of the inverted backscatter-coefficient population when the uncertainties follow a Gaussian distribution (Fig. 8b).

6. CONCLUSIONS

Two different types of backscatter-coefficient inversion error bounds have been formulated: first-order error bounds (Sect. 3) and total-increment error bounds (Sect. 4). Both have been formulated analytically in explicit form for the two-component KFS lidar inversion algorithm subject to error sources 1-4. The error bounds have been validated using a MC method.

First-order error bounds are obtained using the classic error-propagation approach. They are symmetric about the true value with an amplitude lying between those of the upper and lower MC error bounds. Their amplitudes encompass most of the inverted backscatter-profile population in practical situations ($SNR \geq 5$, lidar-ratio relative error strength, $p \leq 30\%$, Sect. 5). Yet, strictly speaking, first-order error bounds are still approximate. With larger errors (lower SNRs and/or higher uncertainties), upper and lower MC error bounds become progressively asymmetric, a property that first-order error bounds cannot reflect.

It has been shown that when the error source follows a Gaussian distribution, total-increment error bounds computed at 3σ coincide with 3-σ statistical confidence levels and, therefore, provide the exact result in explicit analytical form. The total-increment error bound associated with error source 3 was not found explicitly because of the multi-dimensionality of the problem. However, it is well approximated by the 3-σ first-order error bound as $\varepsilon_{j,3}^{u/l} \approx 3\sigma_{\varepsilon_{j,3}}$. Alternatively, when the uncertainty of an error source is assumed to be uniform (the usual case for error sources 1-2 when no further “a priori” information is available) the total-increment error bound gives the total error span on the inverted-backscater profiles.

As in the KLT algorithm, the effect of noise at the calibration cell dominates (particularly towards the NIR) over the effect of the noise from all other range cells. Error sources 1 and 4 are equivalent via (11), thus error sources 2 and 4 are of most concern. Concerning their spectral behavior, uncertainties in the lidar ratio largely dominate the UV error bounds while the backscatter-coefficient calibration is the dominant error source in the NIR. The explicit analytical error bound formulation summarised in Tab. 3 and Tab. 4 is -to the best of our knowledge- new in the state of the art of lidar inversion algorithms.

ACKNOWLEDGEMENTS

This work was supported by the European Union under the project ACTRIS (Aerosols, Clouds, and Trace gases Research Infrastructure Network) ref. nº FP7- INFRA-2010-1.1.16, the European Space Agency under the project 21487/08/NL/HE, the Spanish Ministry of Science and Innovation (MICINN) and FEDER (European Regional Development) funds under the project TEC2009-09106 and Complementary Actions CGL2009-08031-E/CLI ("Charmex") and CGL2008-01330-E/CLI. MICINN and MAEC-AECID (Spanish Ministry of Foreign Affairs and Cooperation) are respectively thanked for Mr. Kumar's and Mr. Lange's predoctoral fellowships.

Thanks also go to three unknown reviewers who helped improving the paper towards a two-component atmosphere, a multi-wavelength approach, and careful structuration of the paper.

APPENDIX: Error propagation due to the (range-dependent) lidar ratio

In (10), the term $\varepsilon_{j,2} = \sum_{k=1}^{N} \frac{\partial \beta_j}{\partial S_k} dS_k$ expresses the back-propagated backscatter-coefficient error due to range-dependent lidar-ratio errors, dS_k. To derive the error bounds we depart from the modified KFS form of (4), and express the lidar-ratio-induced backscatter-coefficient error, $\varepsilon_{j,2}$, as a function of partial derivatives of F_j and H_j

$$\varepsilon_{j,2} = \sum_{k=1}^{N} \frac{\partial \beta_j}{\partial S_k} dS_k = \sum_{k=1}^{N} \frac{\partial \beta_j}{\partial F_j} \frac{\partial F_j}{\partial S_k} dS_k + \sum_{k=1}^{N} \frac{\partial \beta_j}{\partial H_j} \left(\frac{\partial H_j}{\partial S_k} + \sum_{p=1}^{N} \frac{\partial H_j}{\partial F_p} \frac{\partial F_p}{\partial S_k} \right) dS_k \,, \qquad (22)$$

where

$$\frac{\partial \beta_j}{\partial F_j} = \frac{\beta_j}{F_j} \text{ and } \frac{\partial \beta_j}{\partial H_j} = -\frac{2\beta_j^2}{U_j F_j} \,. \qquad (23)$$

Next, $F_j\left(\vec{S}\right)$ and $H_j\left(\vec{S},\vec{U},\vec{F}\right)$ dependency on the lidar ratio is expanded. The dependency of $F_j\left(\vec{S}\right)$ on the lidar ratio is

$$\frac{\partial F_j}{\partial S_k} = \frac{\partial F_j}{\partial G_j} \frac{\partial G_j}{\partial S_k}, \; \frac{\partial F_j}{\partial G_j} = 2F_j \text{, and } \frac{\partial G_j}{\partial S_k} = \begin{cases} 0 & k < j \\ w_k \beta_k^{mol} & k \geq j \end{cases}, \qquad (24)$$

where (6)-(7) have been used. The dependency of $H_j\left(\vec{S},\vec{U},\vec{F}\right)$ on the lidar ratio is

$$\frac{\partial H_j}{\partial S_k} = \begin{cases} 0 & k < j \\ w_k U_k F_k & k \geq j \end{cases} \text{ and } \frac{\partial H_j}{\partial F_p} = \begin{cases} 0 & p < j \\ w_p S_p U_p & p \geq j \end{cases}, \qquad (25)$$

where the definition of H_j in (8) has been used.

From these expressions, (22) can be rewritten in terms of the low-level derivatives (i.e., $\frac{\partial \beta_j}{\partial F_j}$, $\frac{\partial \beta_j}{\partial H_j}$, $\frac{\partial F_j}{\partial G_j}$, $\frac{\partial G_j}{\partial S_k}$, and $\frac{\partial H_j}{\partial S_k}$, $\frac{\partial H_j}{\partial F_p}$) resulting in

$$\varepsilon_{j,2} = \frac{\partial \beta_j}{\partial F_j}\frac{\partial F_j}{\partial G_j}\sum_{k=j}^{N}\frac{\partial G_j}{\partial S_k}dS_k + \frac{\partial \beta_j}{\partial H_j}\sum_{k=j}^{N}\frac{\partial H_j}{\partial S_k}dS_k + \frac{\partial \beta_j}{\partial H_j}\sum_{p=j}^{N}\left(\frac{\partial H_j}{\partial F_p}\frac{\partial F_p}{\partial G_p}\sum_{k=p}^{N}\frac{\partial G_p}{\partial S_k}dS_k\right). \quad (26)$$

Finally, by substituing (23)-(25) into (26) above, the sought-after (28) in Tab. 2 is obtained. The auxiliary integral terms, $dI_{j,1-3}$ in (29)-(31) from Tab. 2 can immediately be identified with terms in (26): $\sum_{k=j}^{N}\frac{\partial G_j}{\partial S_k}dS_k$, $\sum_{k=j}^{N}\frac{\partial H_j}{\partial S_k}dS_k$, and $\frac{1}{2}\sum_{p=j}^{N}\left(\frac{\partial H_j}{\partial F_p}\frac{\partial F_p}{\partial G_p}\sum_{k=p}^{N}\frac{\partial G_p}{\partial S_k}dS_k\right)$, respectively.

As a result, not only lidar ratio errors propagate backward but also an integrated version of them via $\vec{F}(\vec{S})$ and $\vec{H}(\vec{S})$.

FIGURE AND TABLE CAPTIONS

Figures

Fig. 1 Behavior of the forward and backward forms of the KFS-inverted backscatter coefficient for several values of the aerosol lidar ratio. Lidar ratios vary from 20 sr to 80 sr (in steps of 10 sr) in a simulated backscatter profile of an elevated dust layer. Calibration range is at 4 km. For $R < R_{cal}$ inversion is via backward integration and the upper (lower) profile corresponds to the smallest (largest) lidar ratio. For $R > R_{cal}$, inversion is via forward propagation and the upper (lower) profile corresponds to the largest (smallest) lidar ratio.

Fig. 2 Simulated lidar signals. (a) Aerosol backscatter-coefficient atmospheric profiles (solid trace) and related molecular (Rayleigh) levels (dashed). (b) Noisy range-corrected power returns (solid) and related SNR profiles for each channel.

Fig. 3 Analysis of noise corrupting all range cells except the calibration cell (error source 3) for SNR profile in Fig. 2b. (a) Envelopes of the aerosol backscatter coefficient from MC inversion (100 realizations) with superimposed first-order error bounds (vertical error bars) at 3σ. (b) Amplitude of the backscatter-coefficient error bound as a function of range: Comparison between MC error bounds (noisy traces) and first-order error bounds (solid traces). Both (a) and (b) are VIS-normalised.

Fig. 4 Analysis of noise at the calibration range (error source 4) for $SNR(R_{cal}) = 5$, $SNR(R) \to \infty, R \neq R_{cal}$. (a) As in Fig. 3a. (b) First-order error-bound amplitudes at 3σ (thick traces), and asymmetrical MC error-bound amplitudes (thin traces), where solid/dashed traces correspond to

upper/lower MC error bounds, respectively. Total-increment error bounds perfectly match upper and lower MC error bounds and superimpose with them. Both (a) and (b) are VIS-normalised.

Fig. 5 Superposition of error sources 3 and 4. Error amplitude plots comparing total-increment and first-order error bounds with implicit integral error bounds. (a) Perfomance of first-order error bounds: Crosses and circles denote implicit-integral upper and lower error-bound amplitudes at 3σ, respectively, noisy thin solid/dashed traces denote MC upper/lower error amplitudes, respectively, and solid thick traces denote first-order error-bound amplitudes at 3σ. (b) Perfomance of total-increment error bounds: Crosses and circles denote implicit-integral upper and lower error-bound amplitudes at 3σ, respectively, solid lines denote MC upper and lower error-bound amplitudes. Total-increment error bounds perfectly match MC error bounds and superimpose with them.

Fig. 6 Analysis of aerosol backscatter-coefficient calibration error (error source 1). Same description as in Fig. 3a. The family of inverted backscatter-coefficient profiles is in response to a step-function profile of the atmospheric aerosol backscatter coefficient simulating the atmospheric boundary layer ($R \le 5km$). Error strength: ±10% Gaussian fluctuation over the nominal backscatter Rayleigh level at the calibration range ($R_{cal} = R_{\max} = 6km$). Plots are VIS-normalised.

Fig. 7 Analysis of correlated lidar-ratio errors with range (error source 2). (a) Aerosol backscatter-coefficient envelopes from MC inversion with superimposed total-increment error bounds (vertical error bars). Error strength, $p = 30\%$. Uniform fluctuation over the nominal lidar ratio. (b) Backscatter-coefficient error-bound amplitudes associated with (a). Solid trace denotes MC upper/lower error-bound

amplitudes. Total-increment error bounds perfectly match MC error bounds and superimpose with them. Both (a) and (b) are VIS-normalised.

Fig. 8 Performance of total-increment vs. first-order derivative error bounds in the assessment of correlated lidar-ratio errors (error source 2, UV case). Error strength, $p = 30\%$. (a) Total-increment error bounds. Uniform error distribution around the nominal lidar ratio. (b) First-order derivative error bounds. Gaussian fluctuation over the nominal lidar ratio. (a) and (b) plots are VIS-normalised

Tables

Tab. 1 KLT-to-KFS transformation relationships. Notation: In both algorithms, β_j stands for total (aerosol plus molecular) backscatter coefficient at the range cell R_j.

Tab. 2 Total backscatter-coefficient error-propagated terms for the KFS backward inversion algorithm in response to error sources 1-4 (see Sect. 3.1).

Tab. 3 First-order error bounds for the KFS backward inversion algorithm in response to error sources 1-4 (see Sect. 3.2).

Tab. 4 Total-increment error bounds for the KFS backward inversion algorithm in response to error sources 1-4 (see Sect. 4). Superindexes “u” and “l” stand for “upper” and “lower” error bound, respectively. $\varepsilon^{u}_{j,1-4}$ and $\varepsilon^{l}_{j,1-4}$ are positive-defined error amplitudes.

FIGURES

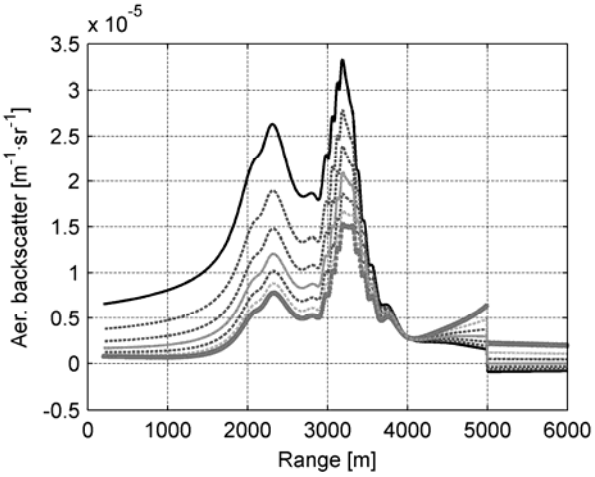

Fig. 1 Behavior of the forward and backward forms of the KFS-inverted backscatter coefficient for several values of the aerosol lidar ratio. Lidar ratios vary from 20 sr to 80 sr (in steps of 10 sr) in a simulated backscatter profile of an elevated dust layer. Calibration range is at 4 km. For $R < R_{cal}$ inversion is via backward integration and the upper (lower) profile corresponds to the smallest (largest) lidar ratio. For $R > R_{cal}$, inversion is via forward propagation and the upper (lower) profile corresponds to the largest (smallest) lidar ratio. Simulation wavelength: 355 nm.

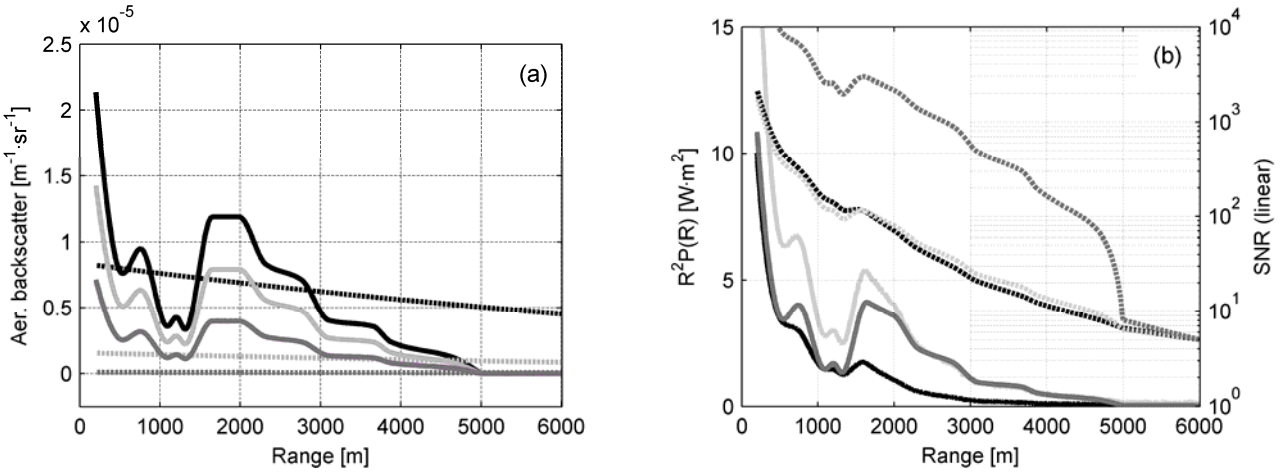

Fig. 2 Simulated lidar signals. (a) Aerosol backscatter-coefficient atmospheric profiles (solid trace) and related molecular (Rayleigh) levels (dashed). (b) Noisy range-corrected power returns (solid) and related SNR profiles for each channel. UV (355 nm, black), VIS (532 nm, light grey), and NIR (1064 nm, dark grey).

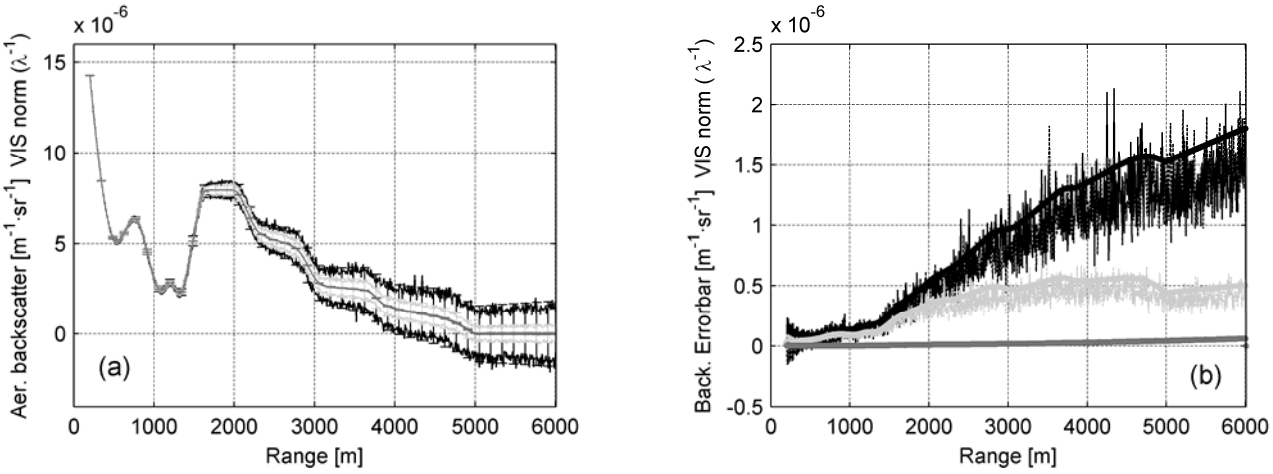

Fig. 3 Analysis of noise corrupting all range cells except the calibration cell (error source 3) for SNR profile in Fig. 2b. (a) Envelopes of the aerosol backscatter coefficient from MC inversion (100 realizations) with superimposed first-order error bounds (vertical error bars) at 3σ. (b) Amplitude of the backscatter-coefficient error bound as a function of range: Comparison between MC error bounds (noisy traces) and first-order error bounds (solid traces). Both (a) and (b) are VIS-normalised.

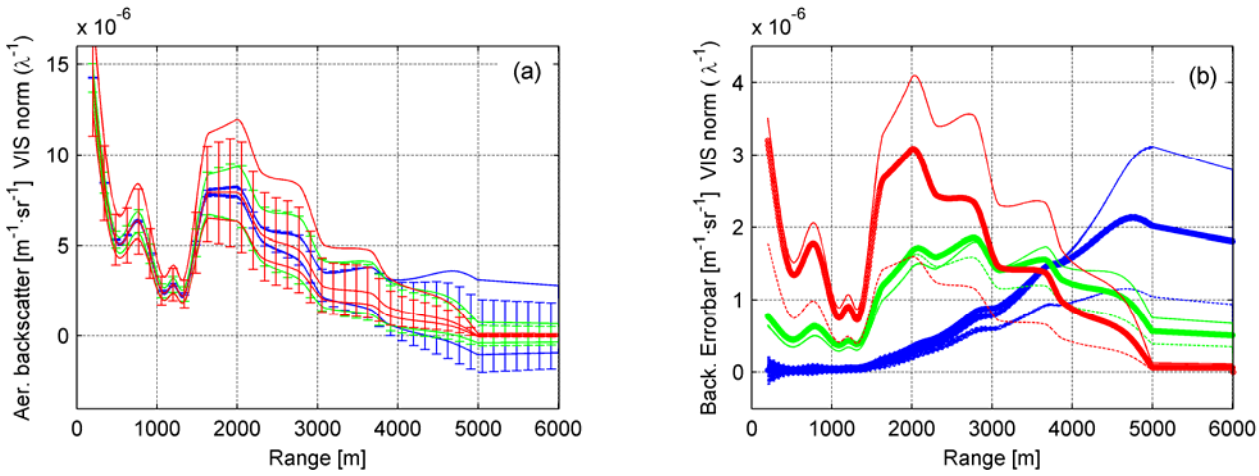

Fig. 4 Analysis of noise at the calibration range (error source 4) for $SNR(R_{cal}) = 5$, $SNR(R) \to \infty$, $R \neq R_{cal}$. (a) As in Fig. 3a. (b) First-order error-bound amplitudes at 3σ (thick traces), and asymmetrical MC error-bound amplitudes (thin traces), where solid/dashed traces correspond to upper/lower MC error bounds, respectively. Total-increment error bounds perfectly match upper and lower MC error bounds and superimpose with them. Both (a) and (b) are VIS-normalised. UV (355 nm, blue), VIS (532 nm, green), and NIR (1064 nm, red).

Reproduction review: Color Figures.

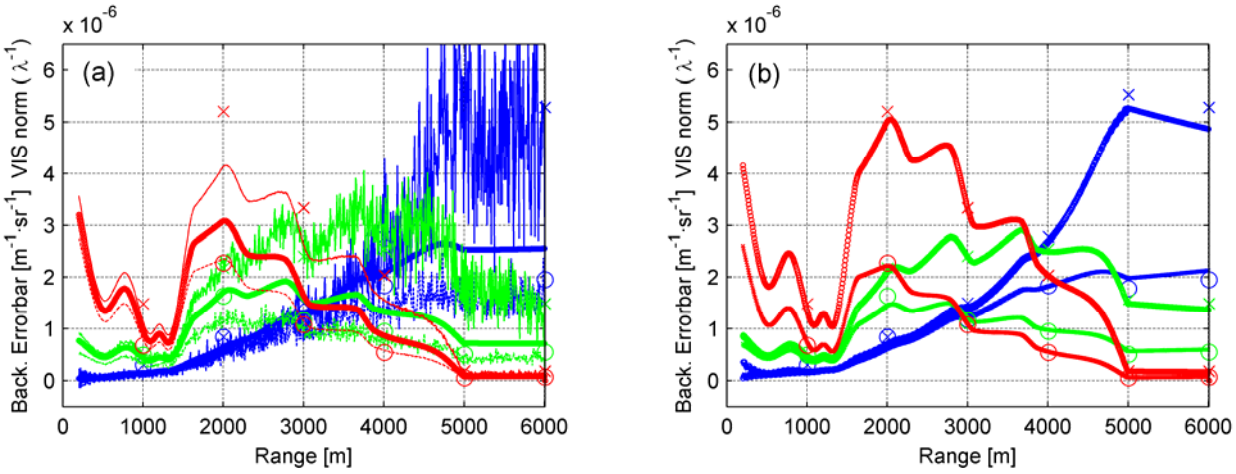

Fig. 5 Superposition of error sources 3 and 4. Error amplitude plots comparing total-increment and first-order error bounds with implicit integral error bounds. (a) Perfomance of first-order error bounds: Crosses and circles denote implicit-integral upper and lower error-bound amplitudes at 3σ, respectively, noisy thin solid/dashed traces denote MC upper/lower error amplitudes, respectively, and solid thick traces denote first-order error-bound amplitudes at 3σ. (b) Perfomance of total-increment error bounds: Crosses and circles denote implicit-integral upper and lower error-bound amplitudes at 3σ, respectively, solid lines denote MC upper and lower error-bound amplitudes. Total-increment error bounds perfectly match MC error bounds and superimpose with them. (a) and (b) plots are VIS-normalised.

Reproduction review: Color Figures.

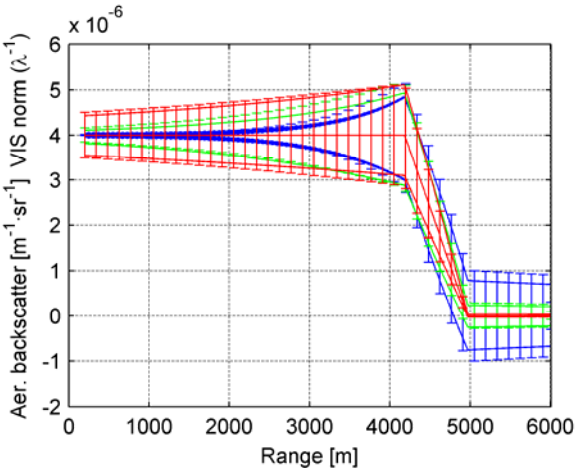

Fig. 6 Analysis of aerosol backscatter-coefficient calibration error (error source 1). Same description as in Fig. 3a. The family of inverted backscatter-coefficient profiles is in response to a step-function profile of the atmospheric aerosol backscatter coefficient simulating the atmospheric boundary layer ($R \le 5km$). Error strength: ±10% Gaussian fluctuation over the nominal backscatter Rayleigh level at the calibration range ($R_{cal} = R_{\max} = 6km$). Plots are VIS-normalised.

Reproduction review: Color Figures.

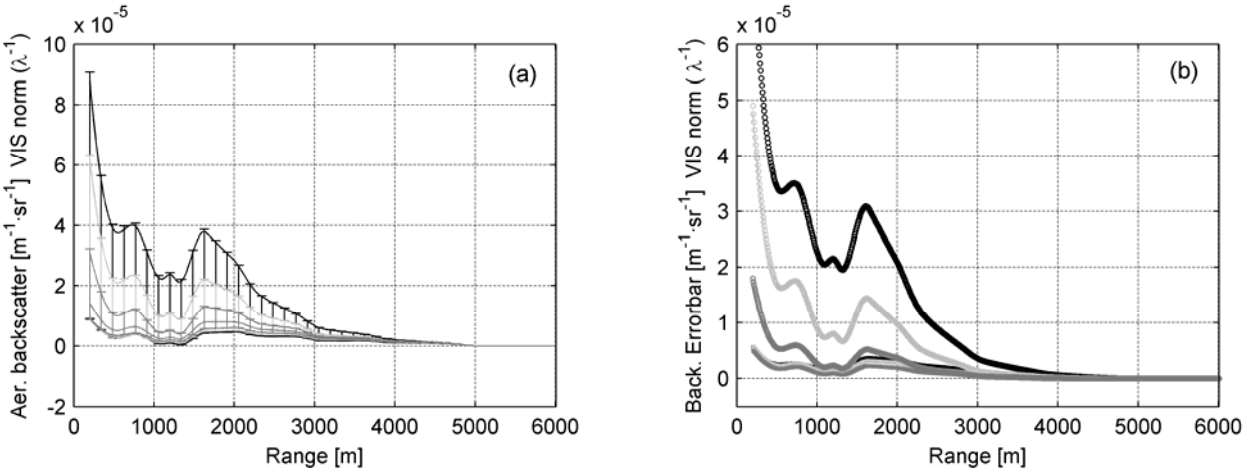

Fig. 7 Analysis of correlated lidar-ratio errors with range (error source 2). (a) Aerosol backscatter-coefficient envelopes from MC inversion with superimposed total-increment error bounds (vertical error bars). Error strength, $p = 30\%$. Uniform fluctuation over the nominal lidar ratio. (b) Backscatter-coefficient error-bound amplitudes associated with (a). Solid trace denotes MC upper/lower error-bound amplitudes. Total-increment error bounds perfectly match MC error bounds and superimpose with them. Both (a) and (b) are VIS-normalised.

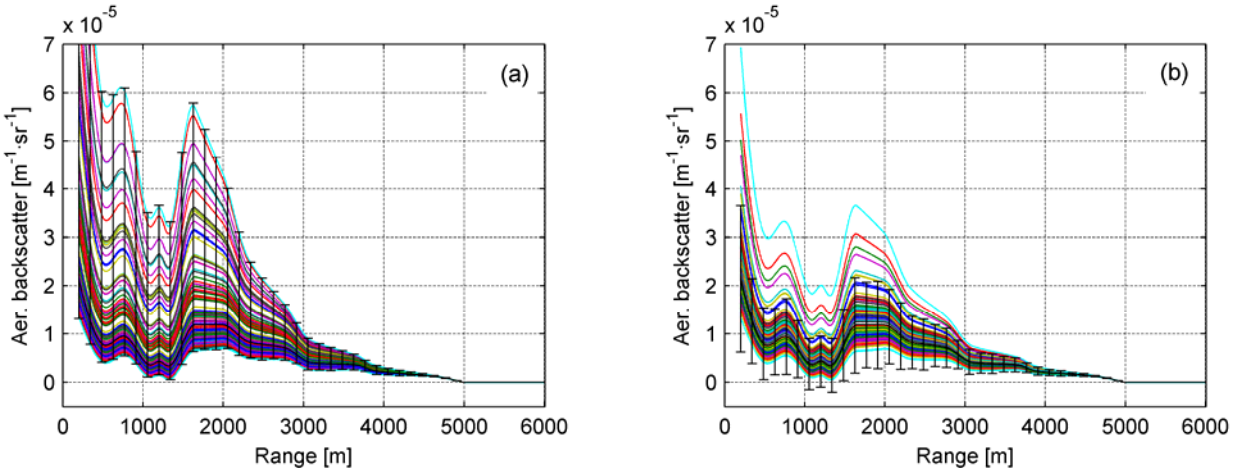

Fig. 8 Performance of total-increment vs. first-order derivative error bounds in the assessment of correlated lidar-ratio errors (error source 2, UV case). Error strength, $p = 30\%$. (a) Total-increment error bounds. Uniform error distribution around the nominal lidar ratio. (b) First-order derivative error bounds. Gaussian fluctuation over the nominal lidar ratio. (a) and (b) plots are VIS-normalised.

Reproduction review: Color Figures.

TABLES

KLT	KFS
$\beta_j\left(\beta_N,\vec{S},\vec{U}\right)=\frac{\beta_N U_j}{U_N+2\beta_N G_j\left(\vec{S},\vec{U}\right)}$	$\beta_j\left(\beta_N,\vec{S},\vec{U}\right)=\frac{\beta_N U_j F_j\left(\vec{S}\right)}{U_N+2\beta_N H_j\left(\vec{S},\vec{U}\right)}$
$\vec{S}$ stands for the total lidar ratio, $\vec{S}^{tot}$	$\vec{S}$ stands for the aerosol lidar ratio, $\vec{S}^{aer}$
U_j	$U_j F_j\left(\vec{S}\right)$
$G_j\left(\vec{S},\vec{U}\right)$	$H_j\left(\vec{S},\vec{U},\vec{F}\right)$

Tab. 1 KLT-to-KFS transformation relationships. Notation: In both algorithms, β_j stands for total (aerosol plus molecular) backscatter coefficient at the range cell R_j.

CONCEPT	FORMULA	EQ.
Total backscatter-coefficient error (case $j < N$) where	$\left\|d\beta_j\right\| = \left\|\frac{\partial\beta_j}{\partial\beta_N}d\beta_N\right\| + \sum_{k=1}^{N}\left\|\frac{\partial\beta_j}{\partial S_k}dS_k\right\| + \sum_{k=1}^{N-1}\left\|\frac{\partial\beta_j}{\partial P_k}dP_k\right\| + \left\|\frac{\partial\beta_j}{\partial P_N}dP_N\right\|; \quad j < N$	(10)
1. Error due to the backscatter-coeffcient calibration	$\varepsilon_{j,1} = \frac{\partial\beta_j}{\partial\beta_N}d\beta_N = \left(\frac{\beta_j}{\beta_N}\right)^2 \frac{U_N}{U_j F_j}d\beta_N$	(27)
2. Error due to the (range-dependent) lidar ratio	$\varepsilon_{j,2} = \sum_{k=1}^{N}\frac{\partial\beta_j}{\partial S_k}dS_k = 2\beta_j dI_{j,1} - \frac{2\beta_j^2}{U_j F_j}dI_{j,2} - \frac{4\beta_j^2}{U_j F_j}dI_{j,3}$	(28)
where	$dI_{j,1} = \sum_{k=j}^{N} w_k \beta_k^{mol} dS_k$	(29)
	$dI_{j,2} = \sum_{k=j}^{N} w_k U_k F_k dS_k$	(30)
	$dI_{j,3} = \sum_{k=j}^{N} w_k S_k U_k F_k dI_{k,1}$	(31)
3. Error due to the measurement noise (range cells 1..N-1)	$\varepsilon_{j,3} = \sum_{k=1}^{N-1}\frac{\partial\beta_j}{\partial P_k}dP_k = \frac{\beta_j}{U_j}dU_j - \frac{2\beta_j^2}{U_j F_j}\sum_{k=j}^{N} w_k S_k F_k dU_k$	(32)
4. Error due to the measurement noise at	$\varepsilon_{j,4} = \frac{\partial\beta_j}{\partial P_N}dP_N = -\frac{\beta_j^2}{\beta_N U_j F_j}dU_N - \frac{2\beta_j^2}{U_j F_j} w_N S_N dU_N$	(33)

the calibration cell (range cell N)		
Total backscatter-coefficient error (case $j = N$, calibration point)	$\left\|d\beta_j\right\| = \left\|d\beta_N\right\|; \qquad j = N$	

Tab. 2 Total backscatter-coefficient error-propagated terms for the KFS backward inversion algorithm in response to error sources 1-4 (see Sect. 3.1). For the case $j = N$, the total backscatter-coefficient error is directly the calibration error. For the KFS forward algorithm consider Sect. 2.4 changes.

CONCEPT	FORMULA	EQ.
Total backscatter-coefficient error bound (case $j < N$) where	$\sigma_{\beta_j} = \left(\sigma^2_{\varepsilon_{j,1}} + \sigma^2_{\varepsilon_{j,2}} + \sigma^2_{\varepsilon_{j,3}} + \sigma^2_{\varepsilon_{j,4}}\right)^{\frac{1}{2}}$,	(34)
1. Error due to the backscatter-coefficient calibration	$\sigma_{\varepsilon_{j,1}} = \left\| \left(\frac{\beta_j}{\beta_N}\right)^2 \frac{U_N}{U_j F_j} \right| \sigma_{\beta_N}$	(35)
2. Error due to the (range-dependent) lidar ratio (correlated case)	$\sigma^C_{\varepsilon_{j,2}} = \|p\| \left\| 2\beta_j I_{j,1} - \frac{2\beta_j^2}{U_j F_j} I_{j,2} - \frac{4\beta_j^2}{U_j F_j} I_{j,3} \right\|$	(36)
where	$I_{j,1} = \sum_{k=j}^{N} w_k \beta_k^{mol} S_k$	(37)
	$I_{j,2} = \sum_{k=j}^{N} w_k U_k F_k S_k$	(38)
	$I_{j,3} = \sum_{k=j}^{N} w_k S_k U_k F_k I_{k,1}$	(39)
(uncorrelated case)	$\sigma_{\varepsilon_{j,2}} = \left[\left(2\beta_j\right)^2 \sigma^2_{I_{1,j}} + \left(\frac{2\beta_j^2}{U_j F_j}\right)^2 \sigma^2_{I_{2,j}} + \left(\frac{4\beta_j^2}{U_j F_j}\right)^2 \sigma^2_{I_{3,j}} \right]^{\frac{1}{2}}$	(40)
where	$\sigma^2_{I_{1,j}} = \sum_{k=j}^{N} \left(w_k \beta_k^{mol}\right)^2 \sigma^2_{S_k}$	(41)

	$\sigma_{I_{2,j}}^2 = \sum_{k=j}^{N} \left(w_k U_k F_k\right)^2 \sigma_{S_k}^2$	(42)
	$\sigma_{I_{3,j}}^2 = \sum_{k=j}^{N} \left(w_k S_k U_k F_k\right)^2 \sigma_{I_{1,k}}^2$	(43)
3. Error due to the measurement noise (range cells 1..N-1)	$\sigma_{\varepsilon_{j,3}} = \left[\left(\frac{\beta_j}{U_j} \right)^2 \sigma_{U_j}^2 + \left(\frac{2\beta_j^2}{U_j F_j} \right)^2 \sigma_{HU,j}^2 \right]^{\frac{1}{2}}$	(44)
where	$\sigma_{HU,j}^2 = \sum_{k=j}^{N} \left(w_k S_k F_k\right)^2 \sigma_{U_k}^2$	(45)
4. Error due to the measurement noise at the calibration cell (range cell N)	$\sigma_{\varepsilon_{j,4}} = \left(\left\| \frac{\beta_j^2}{\beta_N U_j F_j} \right\| + \left\| \frac{2\beta_j^2}{U_j F_j} w_N S_N \right\| \right) \sigma_{U_N} \approx \approx \left\| \frac{\beta_j^2}{\beta_N U_j F_j} \right\| \sigma_{U_N}$	(46)
Total backscatter-coefficient error bound (case $j = N$, calibration point)	$\sigma_{\beta_j} = \sigma_{\beta_N}$	

Tab. 3 First-order error bounds for the KFS backward inversion algorithm in response to error sources 1-4 (see Sect. 3.2). For the case $j = N$, the backscatter-coefficient error bound is directly the calibration error bound. For the KFS forward algorithm consider Sect. 2.4 changes.

CONCEPT	FORMULA	EQ.
Total backscatter-coefficient error bound (case $j < N$) where	$\varepsilon_{tot,j}^{u/l} = \left(\varepsilon_{j,1}^2 + \varepsilon_{j,2}^2 + \varepsilon_{j,3}^2 + \varepsilon_{j,4}^2\right)^{\frac{1}{2}}$	(47)
1. Error due to the backscatter-coefficient calibration $\frac{\partial \beta_j}{\partial \beta_N} > 0$, (27)	$\varepsilon_{j,1}^{u} = \beta_j\left(\beta_N + d\beta_N\right) - \beta_j\left(\beta_N\right)$ $\varepsilon_{j,1}^{l} = -\beta_j\left(\beta_N - d\beta_N\right) + \beta_j\left(\beta_N\right)$ ($d\beta_N = 3\sigma_{\beta_N}$ for 3-σ level)	(48)
2. Error due to the (range-dependent) lidar ratio (correlated case)	$\beta_j(p) = \frac{\beta_N\, U_j F_j(p)}{U_N + 2\beta_N\, H_j\left(p, \vec{U}\right)}$ $\beta_j(p)$ stands for $\beta_j\left(\vec{S} + d\vec{S}\right), d\vec{S} = p\vec{S}$	(49)
Case FORWARD $\frac{\partial \beta_j}{\partial p} > 0$, Sect. 4.2	$\varepsilon_{j,2}^{u} = \beta_j\left(\vec{S} + d\vec{S}\right) - \beta_j\left(\vec{S}\right)$ $\varepsilon_{j,2}^{l} = -\beta_j\left(\vec{S} - d\vec{S}\right) + \beta_j\left(\vec{S}\right)$	(50)
Case BACKWARD $\frac{\partial \beta_j}{\partial p} < 0$, Sect. 4.2	$\varepsilon_{j,2}^{u} = \beta_j\left(\vec{S} - d\vec{S}\right) - \beta_j\left(\vec{S}\right)$ $\varepsilon_{j,2}^{l} = -\beta_j\left(\vec{S} + d\vec{S}\right) + \beta_j\left(\vec{S}\right)$	(51)
3. Error due to the measurement noise (range cells 1..N-1)	(not available) Use $\varepsilon_{j,3}^{u/l} \approx 3\sigma_{\varepsilon_{j,3}}$, 3-σ first-order error	(52)

	approx.	
4. Error due to the measurement noise at the calibration cell (range cell N) $\frac{\partial \beta_j}{\partial P_N} < 0$, (33)	$\varepsilon_{j,4}^{u} = \beta_j(U_N - dU_N) - \beta_j(U_N)$ $\varepsilon_{j,4}^{l} = -\beta_j(U_N + dU_N) + \beta_j(U_N)$ ($dU_N = 3\sigma_{U_N}$ for 3-σ level)	(53)
Total backscatter-coefficient error bound (case $j = N$, calibration point)	$\varepsilon_{tot,j}^{u/l} = \varepsilon_{\beta_N}^{u/l}$	(54)

Tab. 4 Total-increment error bounds for the KFS backward inversion algorithm in response to error sources 1-4 (see Sect. 4). Superindexes “u” and “l” stand for “upper” and “lower” error bound, respectively. $\varepsilon_{j,1-4}^{u}$ and $\varepsilon_{j,1-4}^{l}$ are positive-defined error amplitudes. For the case $j = N$, the upper/lower backscatter-coefficient error bounds are directly given by those of the calibration error. For the KFS forward algorithm consider Sect. 2.4 changes.

REFERENCES

[1] J.A. Reagan, M.P. McCormick, and J.D. Spinhirne, “Lidar Sensing of Aerosols and Clouds in the Troposphere and Stratosphere” (invited paper), *Proc. IEEE,* **77**(3), 433-448, 1989.

[2] F. Rocadenbosch, I. Mattis, C. Böckmann, *G. Pappalardo (PI),* J. Bösenberg, L. Alados-Arboledas, A. Amodeo, A. Ansmann, A. Apituley, D. Balis, A. Chaikovsky, A. Comerón, V. Freudenthaler, O. Gustafsson, G. Hansen, R.E. Mamouri, V. Mitev, C. Muñoz, D. Nicolae, A. Papayannis, C. Pérez, M. R. Perrone, A. Pietruczuk, M. Pujadas, J.P. Putaud, F. Ravetta, V. Rizi, M. Sicard, V. Simeonov, N. Spinelli, D. Stoyanov, T. Trickl, U. Wandinger, M. Wiegner, “The European Aerosol Research Lidar Network (EARLINET): An overview,” (invited paper). International Geoscience and Remote Sensing Symposium (IGARSS-08), Conference on EARLINET -- The European Aerosol Research Lidar Network, Boston (MA, USA), 8 July 2008. *Proc. IEEE Intal. Geosci. Remote Sens. Symp. (IGARSS-08),* II-410 to II-413, ISBN: 978-1-4244-2808-3.

[3] D.M. Winker, R.H. Couch, and P. McCormick, “An overview of LITE: NASA’s Lidar In-Space Technology Experiment,” *Proc. IEEE,* **84**(2) 164-180, 1996.

[4] D.M. Winker and J. Pelon, “The CALIPSO Mission”, *Proc. IEEE Int. Geosci. Remote Sens. Symp., 2003,* Vol. 2, 1329-1331.

[5] R.T.H. Collis and P.B. Russell, "Lidar Measurement of Particles and Gases by Elastic Backscattering and Differential Absorption," Chap.4 in *Laser Monitoring of the Atmosphere,* E.D. Hinkley, Ed., pp. 71-102, (Springer-Verlag, New York, 1976), pp.71-102.

[6] WMO GAW (2007), Plan for the implementation of the GAW Aerosol Lidar Observation Network (GALION) (Hamburg, Germany, 27-29 March 2007) (WMO TD nº 1443).

[7] J.A. Reagan, X. Wang, M.T. Osborn, "Spaceborne lidar calibration from cirrus and molecular backscatter returns," *IEEE Trans. Geosci. Remote Sens.*, **40**(10), 2285- 2290, 2002.

[8] T. Nishizawa, N. Sugimoto, I. Matsui, A. Shimizu, B. Tatarov, H. Okamoto, "Algorithm to Retrieve Aerosol Optical Properties From High-Spectral-Resolution Lidar and Polarization Mie-Scattering Lidar Measurements," *IEEE Trans. Geosci. Remote Sens.*, **46**(12), 4094-4103, 2008.

[9] M. Sicard, P. Chazette, J. Pelon, J. Gwang-Won, and Soon-Chang Yoon, "Variational method for the retrieval of the optical thickness and the backscatter coefficient from multiangle lidar profiles," *Appl. Opt.*, **41** (3), 493-502, 2002.

[10] A. Ansmann, U. Wandinger, M. Riebesell, C. Weitkamp, and W. Michaelis, "Independent measurement of extinction and backscatter profiles in cirrus clouds by using a combined Raman elastic-backscatter lidar," *Appl. Opt.*, **31**(33), 7113-7131, 1992.

[11] W. Hitschfeld and J. Bordan, "Errors inherent in the radar measurement of rainfall at attenuating wavelengths," *J. Appl. Meteor.* **11,** 58-67, 1954.

[12] E. W. Barret and O. Ben-Dov, "Application of the lidar to air pollution measurements," *J. Appl. Meteor.* **6,** 500-515, 1967.

[13] W. Viezee, E.E. Uthe, and R.T.H. Collis, "Lidar observations of airfield approach conditions: an exploration study," *J. Appl. Meteor.* **8,** 274-283, 1969.

[14] P.A. Davis, "The analysis of lidar signatures of cirrus clouds," *Appl. Opt.*, **8**(10), 2099-2102, Oct. 1969.

[15] F.G. Fernald, B.M. Herman, and J.A. Reagan, "Determination of aerosol height distribution by lidar," *J. Appl. Meteor.* **11,** 482-489, 1972.

[16] R.H. Kohl, "Discussion of the interpretation problem encountered in single-wavelength lidar transmissometers," *J. Appl. Meteor.* **17**, 1034-38, 1978.

[17] J.D. Klett, "Stable Analytical Inversion Solution for Processing Lidar Returns," *Appl. Opt.* **20**(2), 211-220, 1981.

[18] F.G. Fernald, "Analysis of Atmospheric Lidar Observations: Some Comments," *Appl. Opt.* **23**(5), 652-3, 1984.

[19] J.D. Klett, "Lidar Inversion with Variable Backscatter/Extinction Ratios," *Appl. Opt.* **24**, 1638-1643, 1985.

[20] J.D. Klett, "Lidar Calibration and Extinction Coefficients," *Appl. Opt.* **20**, 514-515, 1983.

[21] J. D. Klett, "Extinction boundary value algorithms for lidar inversion", *Appl. Opt.,* **25**(15), 2462-2464, 1986.

[22] Y. Sasano and H. Nakane, "Quantitative Analysis of RHI Lidar Data by an Iterative Adjustment of the Boundary Condition Term in the Lidar Solution," *Appl. Opt.* **26**(4), 615-6, 1987.

[23] Y.Sasano and H. Nakane, "Significance of the Extinction/Backscatter Ratio and the Boundary Value Term in the Solution for the Two-Component Lidar Equation," *Appl. Opt.* **23**(1), 11-13, 1984.

[24] Y. Sasano, E. V. Browell, and S. Ismail, "Error Caused by Using a Constant Extinction/Backscattering Ratio in the Lidar Solution," *Appl. Opt.* **24**(22), 3929-3932, 1985.

[25] L.R. Bissonnette, "Sensitivity Analysis of Lidar Inversion Algorithms," *Appl. Opt.* **25**(13), 2122-2125, 1986.

[26] M. Matsumoto and N. Takeuchi, "Effects of misestimated far-end boundary values on two common lidar inversion solutions," *Appl. Opt.* **33**(27), 6451-6456, 1994.

[27] J. Qiu, "Sensitivity of lidar equation solution to boundary values and determination of the values," *Adv. Atmos. Sci.* **5**(2), 229-241, 1988.

[28] A. Ansmann, "Ground-truth aerosol lidar observations: Can the Klett solutions obtained from ground and space be equal for the same aerosol scenario?", *Appl. Opt.*, **45**, 3367-3371, 2006.

[29] G.J. Kunz, "Transmission as an input boundary value for an analytical solution of a single-scatter lidar equation," *Appl. Opt.* **35**(18), 3255-3260, 1996.

[30] V.A. Kovalev, "Lidar measurement of the vertical aerosol extinction profiles with range-dependent backscatter-to-extinction ratios," *Appl. Opt.* **32**(30), 6053-6065, 1993.

[31] V.A. Kovalev, "Stable near-end solution of the lidar equation for clear atmospheres," *Appl. Opt.* **42**(3), 585-591, 2003.

[32] M.N. Md. Reba, F. Rocadenbosch, M. Sicard, D. Kumar, and S. Tomás, "On the lidar ratio estimation from the synergy between aeronet sun-photometer data and elastic lidar inversion," 25th International Laser Radar Conference (ILRC25) (Session S9 on Combining Lidar with Other Techniques and Unique Lidar Applications), St. Petersburg (Russia), 5-9 Jul. 2010. Proc. ILRC25, Vol. 2, pp. 883-886, (2010). ISBN 978-5-94458-109-9.

[33] G.L. Stephens and R.J. Engelen, "Toward retrieving properties of the tenuous atmosphere using space-based lidar measurements," *J. Geophys. Rsch.,* **106** (D22), 28.143-28.157, 2001.

[34] F. Rocadenbosch, C. Soriano, A. Comerón, and J.M. Baldasano, "Lidar inversion of atmospheric backscatter and extinction-to-backscatter ratios by use of a Kalman filter," *Appl. Opt.,* **38**(15), 3175-3189, 1999.

[35] C.C. Marchant, T.K. Moon, J.H. Gunther, "An Iterative Least Square Approach to Elastic-Lidar Retrievals for Well-Characterized Aerosols," *IEEE Trans. Geosci. Remote Sens.*, **48**(5), 2430-2444, 2010.

[36] N. Huneeus and O. Boucher, "One-dimensional variational retrieval of aerosol extinction coefficient from synthetic LIDAR and radiometric measurements," *J. Geophys. Rsch.,* **112** (D14303), doi: 10.1029/2006JD007625, 2007.

[37] C. Böckmann, D. Müller, L. Osterloh, P. Pornsawad, and A. Papayannis, "From EARLINET-ASOS Raman-Lidar signals to microphysical aerosol properties via advances regularizing

software," *Proc. IEEE Intal. Geosci. Remote Sens. Symp.* (IGARSS 2008), pp. (II-422)-(II-425), 2008.

[38] F. Rocadenbosch and A. Comerón, "Error Analysis For The Lidar Backward Inversion Algorithm," *Appl. Opt.* **38**(21), 4461-4474, 1999.

[39] A. Comerón, F. Rocadenbosch, M. A. López, A. Rodríguez, C. Muñoz, D. García-Vizcaíno, and M. Sicard, "Effects of noise on lidar data inversion with the backward algorithm", *Appl. Opt.* **43**(12), 2572-2577, 2004.

[40] F. Rocadenbosch, M.N. Md. Reba, M. Sicard, and A. Comerón, "Practical analytical backscatter error bars for the elastic one-component lidar inversion algorithm", *Appl. Opt.*, **49**(17), 3380-3393, 2010.

[41] M. Sicard, A. Comerón, F. Rocadenbosch, A. Rodríguez, and C. Muñoz, "Quasi-analytical determination of noise-induced error limits in lidar retrieval of aerosol backscatter coefficient by the Klett-Fernald-Sasano algorithm", *Appl. Opt.* **48**(2), 176-182, 2009.

[42] B.A. Bodhaine, N.B. Wood, E.G. Dutton, and J.R. Slusser, "On Rayleigh Optical Depth Calculations," *J. Atmos. Ocean. Tech.* **16**(11), 1854-1861, 1999.

[43] R. Barlow, "Errors," Chap. 4 in *Statistics. A Guide to the Use of Statistical Methods in Physical Sciences* (Wiley, Chichester, England, 1999), pp. 48-67.

[44] D.C. Knauss, "Significance of the boundary value term in the Klett lidar inversion formula," *Appl. Opt.* **21**(23), 4194, 1982.

[45] F. Rocadenbosch, M. N. Md. Reba, M. Sicard, S. Tomás, and D. Kumar, "Lidar ratio estimation using a two-point calibration in a turbid layer aloft," 25th International Laser Radar Conference (ILRC25) (Session S1 on Advances in Lidar Components and Techniques), St. Petersburg (Russia), 5-9 Jul. 2010. Proc. ILRC25, Vol. 1, pp. 59-62, (2010). ISBN 978-5-94458-109-9.

[46] F. Rocadenbosch, A. Comerón, and D. Pineda, “Assessment of lidar inversion errors for homogeneous atmospheres,” *Appl. Opt.* **37**(12), 2199-2206, 1998.